fluids

MDPI

Article

Numerical Investigation of the Influence of Temperature on Fluidization Behavior: Importance of Particle Collision Parameters and Inter-Particle Forces

Milan Mihajlović [1], Juan G. Ramírez [1,2], Ildefonso Campos Velarde [1], Martin Van Sint Annaland [1,2] and Ivo Roghair [1,2,*]

[1] Chemical Process Intensification Group, Department of Chemical Engineering and Chemistry, Eindhoven University of Technology, 5600 MB Eindhoven, The Netherlands; mmihajlovic89@yahoo.com (M.M.); j.g.ramirez.hernandez@tue.nl (J.G.R.); ildefonsocampos@yahoo.com (I.C.V.); m.v.sintannaland@tue.nl (M.V.S.A.)

[2] Eindhoven Institute of Renewable Energy Systems (EIRES), Eindhoven University of Technology, 5600 MB Eindhoven, The Netherlands

* Correspondence: i.roghair@tue.nl

Abstract: Fluidized bed reactors (FBRs) are integral to various industries due to their exceptional capability in facilitating efficient gas–solid interactions, resulting in superior mixing and heat and mass transfer. This research delves into the impact of temperature on fluidization dynamics, particularly focusing on the collisional properties of particles within the bed. The investigation builds upon foundational research, notably Geldart's classification of fluidization regimes and recent advancements in high-temperature experimental techniques, such as High-Temperature Endoscopic-Laser particle image velocimetry/digital image analysis. To explore these temperature effects, a coupled Discrete Element Method and Computational Fluid Dynamics (CFD–DEM) model was employed. This approach enables a detailed examination of gas–particle and particle–particle interactions under varying temperature conditions. The simulations in this study explore the friction coefficient, as well as changes in both tangential and normal restitution coefficients, which affect the fluidization behavior. These changes were systematically analyzed to determine their influence on minimum fluidization velocity and bubble formation. The numerical results are compared with experimental data from high-temperature fluidization studies, highlighting the necessity of incorporating inter-particle forces to fully capture the observed phenomena. The findings underscore the critical role of particle collisional properties in high-temperature fluidization and suggest the potential increasing role of inter-particle forces. Overall, this paper provides new insights into the complex dynamics of fluidized beds at elevated temperatures, emphasizing the need for further experimental–numerical research to enhance the reliability and understanding of these systems in industrial applications.

Keywords: discrete particle model; particle collisional properties; high-temperature gas–solid fluidization; inter-particle forces

check for updates

Academic Editor: Lin Tian

Received: 14 January 2025
Revised: 18 February 2025
Accepted: 21 February 2025
Published: 27 February 2025

Citation: Mihajlović, M.; Ramírez, J.G.; Campos Velarde, I.; Van Sint Annaland, M.; Roghair, I. Numerical Investigation of the Influence of Temperature on Fluidization Behavior: Importance of Particle Collision Parameters and Inter-Particle Forces. *Fluids* **2025**, *10*, 60. https://doi.org/10.3390/fluids10030060

Copyright: © 2025 by the authors. Licensee MDPI, Basel, Switzerland. This article is an open access article distributed under the terms and conditions of the Creative Commons Attribution (CC BY) license (https://creativecommons.org/licenses/by/4.0/).

1. Introduction

Fluidized bed reactors (FBRs) are pivotal in numerous industries due to their exceptional capability to facilitate efficient gas–solid interactions. These reactors excel in achieving superior solid mixing and excellent heat and mass transfer across phases. FBRs are widely applied across various sectors, including the chemical, pharmaceutical, food, oil, and metal industries, each utilizing these reactors under diverse operational conditions.

Extensive research has explored the effects of varying operational conditions and particle characteristics on fluidization. This exploration began notably with Geldart's seminal 1973 work, which classified fluidization regimes based on particle size and gas properties [1]. In this study, we focus on understanding the impact of temperature on fluidization behavior. This is a highly relevant topic that has been investigated through both experimental and numerical approaches [2–6]. Notably, advancements in high-temperature materials and optics have enabled detailed hydrodynamic studies, such as the High-Temperature Endoscopic-Laser PIV/DIA (Particle Image Velocimetry coupled with Digital Image Analysis [7]) method presented by Campos Velarde [8]. This technique provided unprecedented visual insights into high-temperature fluidization, suggesting a significant role of particle collisional properties—like normal and tangential restitution coefficients and particle friction coefficients—in fluidization dynamics, apart from the changes in the gas properties.

Their results included two experiments performed at different temperatures while managing to use the same gas phase density and viscosity by changing the gas composition. To their surprise, despite the equal gas phase properties, the fluidization behavior was notably different. This suggests that, aside from the commonly accepted influence of the gas phase properties, the change in temperature poses an additional and significant influence on the way that particles interact. Two alternative phenomena promoted by higher temperatures are Van der Waals interactions (VDW), as discussed in, e.g., Mihajlovic et al. [6], and changes in contact (collisional) properties, such as the coefficients for normal and tangential restitution and particle friction. The strength of the Van der Waals force increases as the molecular dipole pulsation around the contact point increases with temperature [9]. The temperature dependence of the collision parameters can be related to changes in the mechanical properties of the solids [10,11]. Previously, Mihajlovic et al. [6] numerically evaluated the effect of VDW interactions on fluidization at high temperatures. To the best of the authors' knowledge, the impact of temperature-dependent collision parameters on fluidization behavior has not been investigated in detail, making it the focus of this paper.

Particle collisional properties are temperature-dependent, varying across materials [10]. As the operating temperature rises, changes in the friction coefficients of materials occur, impacting particle behavior in fluidized systems. Previous studies [11–13] have shown that, with increasing temperature, the restitution coefficient generally decreases, although this behavior is strongly dependent on the type of material. Some analyses even suggest that restitution coefficients may alter trends based on changing conditions [14,15]. In this study, it is hypothesized that increasing temperature results in higher friction coefficients and decreasing tangential and normal restitution coefficients for spherical particles in fluidized beds, causing the collisions to become less elastic.

Given the complexity of these detailed interactions, we employ a numerical approach using the Discrete Element Method coupled with Computational Fluid Dynamics (CFD–DEM). This coupled method enables comprehensive simulations of gas–particle and particle–particle interactions in fluidized beds. The CFD–DEM is particularly effective in adjusting particle collisional properties and provides valuable insights into the bed's hydrodynamics, including energy dissipation and the detailed behavior of individual particles. Previous CFD–DEM studies of fluidized beds at high temperatures have primarily focused on characterizing the heat transfer within the bed [16–19] or temperature-induced adhesion and sintering [20–22]. However, a clear understanding of how temperature-induced changes in collision parameters affect fluidization behavior remains lacking.

The remainder of this article is organized as follows:

- A deeper exploration of our numerical model will be presented in the initial section of this paper, with a focus on the DEM part of the code.

- Subsequently, we present an investigation regarding the general influence of each collisional parameter on fluidization conditions, expanding on Laverman's earlier work [23]. By utilizing a broader range of values in our CFD–DEM simulations, we explore the effects of these parameters on the minimum fluidization velocity and bubble formation. Single-bubble injection cases are also analyzed to understand how collisional parameters might influence bubble size during full fluidization.
- At the end of this paper, a numerical investigation on the experimental findings of Campos Velarde [8] was performed. The simulations replicated the experimental conditions, incorporating exact gas properties and adjusted particle collisional properties to achieve comparable results. The determination of the minimum fluidization velocities occurred by varying these parameters and subsequently performing full fluidization simulations to analyze the influence of the particle properties on the bubbling regime.

2. Model Description

The numerical model employed in this study is an in-house Euler–Lagrange method that originates from the works of Hoomans et al. [24], van der Hoef et al. [25], Ye et al. [26] and Tan [27]. The gas flow is resolved on a Eulerian background mesh, composed of Cartesian grid cells, using the volume-averaged Navier–Stokes equations, which constitutes the CFD part of the model. The DEM side corresponds to the particles being tracked as Lagrangian discrete entities following Newton's second law of motion. An important aspect of every DEM representation is the way the contact forces between the particles are modeled, which occurs via a linear spring–dashpot model originally developed by Cundall and Strack [28]. For more information on these equations and their numerical solutions, refer to the mentioned works. In Table 1, the governing equations of the CFD–DEM are presented.

Table 1. Governing equations.

Gas Phase Equations		
Continuity equation	$\frac{\partial(\epsilon_g \rho_g)}{\partial t} + \nabla \cdot (\epsilon_g \rho_g \mathbf{u}_g) = 0$	(1)
Navier–Stokes momentum equation	$\frac{\partial(\epsilon_g \rho_g \mathbf{u}_g)}{\partial t} + \nabla \cdot (\epsilon_g \rho_g \mathbf{u}_g \mathbf{u}_g) = -\epsilon_g \nabla P_g - \mathbf{S}_p - \nabla \cdot (\epsilon_g \tau_g) + \epsilon_g \rho_g \mathbf{g}$	(2)
Stress tensor	$\tau_g = \mu_g(\nabla \mathbf{u}_g + \nabla \mathbf{u}_g^T) - (\lambda_g - \frac{2}{3}\mu_g)(\nabla \cdot \mathbf{u}_g)\mathbf{I}$	(3)
Interface momentum exchange	$\mathbf{S}_p = \frac{1}{V} \sum_{\forall a \in V} \frac{V_a \beta}{1 - \epsilon_g}(\mathbf{u}_g - \mathbf{v}_a) D(\mathbf{r} - \mathbf{r}_a)$	(4)
Porosity in Eulerian cell	$\epsilon_{g,cell} = 1 - \frac{1}{V_{cell}} \sum_{\forall a \in cell} f^a_{cell} V_a$	(5)
Particle Phase Equations		
Translational motion	$m_a \frac{d\mathbf{v}_a}{dt} = m_a \frac{d^2 \mathbf{r}_a}{dt^2} = \mathbf{F}_{\text{pres gradient}} + \mathbf{F}_{\text{drag}} + \mathbf{F}_{\text{gravity}} + \mathbf{F}_{\text{contact,a}} + \mathbf{F}_{\text{inter-particle,a}}$	(6)
Rotational motion	$I_a \frac{d\omega_a}{dt} = \mathbf{T}_a$	(7)
Inertia tensor	$I_a = \frac{2}{5} m_a R_a^2$	(8)
Torque	$\mathbf{T}_a = \sum_{b \in \text{contact list}} (R_a \mathbf{n}_{ab} \times \mathbf{F}_{ab,t})$	(9)

The interaction between the particles and the gas phase in the CFD–DEM is obtained through four-way coupling. The governing equations between the gas and particle phases are coupled through porosity and inter-phase momentum exchange (drag). For the particles, the gas-phase interaction is manifested via the drag force and pressure gradient. In this work, the correlation from Syamlal and Gidaspow [29] for the drag force coefficient was

used. The pressure gradient calculation is performed using a volume-weighing technique using the values of the pressure gradients at the eight surrounding computational nodes. In this paper, the focus is on the discrete particle model part, while the gas phase will be only presented via governing equations. For more details on the gas phase equations and the numerical solution strategy of coupling between particle and gas phase equations, refer to Tan [27].

2.1. Particle Phase

The motion of the particles is modeled using the equations presented in Table 1. The translational motion for a single particle of mass m_a, velocity $\mathbf{v}_a$, and position $\mathbf{r}_a$ is calculated via Newton's second law of motion, and it is provided in Equation (6). The forces acting on the single particles are summed as the total force of the pressure gradient, drag force, gravity, and contact force due to collisions and inter-particle forces. The rotational motion of particle a is described with the angular velocity via Equation (7). The torque is provided by Equation (9), which only depends on the tangential component of the individual particle–particle or particle–wall contact forces.

$$\mathbf{F}_{\text{pressure gradient}} = -V_a \nabla P_g \tag{10}$$

$$\mathbf{F}_{\text{drag}} = \frac{V_a \beta}{1 - \epsilon_g} (\mathbf{u}_g - \mathbf{v}_a) \tag{11}$$

$$\mathbf{F}_{\text{gravity}} = m_a \mathbf{g} \tag{12}$$

2.1.1. Contact Force

The particle collisional properties whose influence is the prime research objective of this research are part of the contact force. They are incorporated in different equations and influence the collision of the particles. Their physical representation is the loss of energy during the collision of particles or particle and wall. All these are represented in the contact force. The contact force in the CFD–DEM accounts for particle–particle and particle–wall interactions of each individual particle a ($\mathbf{F}_{\text{contact,a}}$). This force is divided into a normal and tangential component, presented in Equation (13).

$$\mathbf{F}_{\text{contact,a}} = \sum_{b \in \text{contact list}} (\mathbf{F}_{ab,n} + \mathbf{F}_{ab,t}) \tag{13}$$

Detailed models for an accurate contact force employ complicated mechanics, and the computational time will be quite excessive [30]. Therefore, simplified models have been proposed that use an approximate formulation of the particle–particle or particle–wall contact forces. A simple and accepted implementation is originally developed by Cundall and Strack [28], where normal and tangential components of the contact forces are modeled via a linear spring–dashpot model.

The normal component of the soft-sphere model can be calculated via Equation (14):

$$\mathbf{F}_{ab,n} = -k_n \delta_n \mathbf{n}_{ab} - \eta_n \mathbf{v}_{ab,n} \tag{14}$$

where k_n is the normal spring stiffness, $\mathbf{n}_{ab}$ is the normal unit vector, η_n is the normal damping coefficient, and $\mathbf{v}_{ab,n}$ is the normal relative velocity. The normal restitution

coefficient e_n as one of the key parameters for this study is incorporated in the normal damping coefficient, which is calculated via

$$\eta_n = \begin{cases} \frac{-2\ln e_n \sqrt{m_{\text{eff}} k_n}}{\sqrt{\pi^2 + \ln^2 e_n}} & \text{if } e_n \neq 0 \\ 2\sqrt{m_{\text{eff}} k_n} & \text{if } e_n = 0 \end{cases} \tag{15}$$

The reduced mass m_{eff} for the two interacting particles is provided by

$$\frac{1}{m_{\text{eff}}} = \frac{1}{m_a} + \frac{1}{m_b} \tag{16}$$

The normal overlap, δ_n, is provided by

$$\delta_n = (R_a + R_b) - |\mathbf{r}_a - \mathbf{r}_b| \tag{17}$$

with R_a and R_b representing the radii of particle a and b, respectively. The normal unit vector is defined as

$$\mathbf{n}_{ab} = \frac{\mathbf{r}_b - \mathbf{r}_a}{|\mathbf{r}_b - \mathbf{r}_a|} \tag{18}$$

The relative velocity between particles a and b is provided by Equation (19), where $\mathbf{v}_a$ and $\mathbf{v}_b$ stand for the particle linear velocities and ω_a and ω_b for the angular velocities.

$$\mathbf{v}_{ab} = (\mathbf{v}_a - \mathbf{v}_b) + (R_a\omega_a + R_b\omega_b) \times \mathbf{n}_{ab} \tag{19}$$

The normal component of the relative velocity between particle a and b is calculated via

$$\mathbf{v}_{ab,n} = (\mathbf{v}_{ab} \cdot \mathbf{n}_{ab})\mathbf{n}_{ab} \tag{20}$$

For the tangential component of the contact force, a Coulomb-type friction law is used, which depends on the particle friction coefficient μ_f (see Equation (21)). The tangential restitution coefficient e_t is used in the tangential damping coefficient η_t. k_t is the tangential spring stiffness and δ_t the tangential displacement.

$$\mathbf{F}_{ab,t} = \begin{cases} -k_t\delta_t - \eta_t\mathbf{v}_{ab,t} & \text{if } |\mathbf{F}_{ab,t}| \leq \mu_f|\mathbf{F}_{ab,n}| \\ -\mu_f\,|\mathbf{F}_{ab,n}|\mathbf{t}_{ab} & \text{if } |\mathbf{F}_{ab,t}| > \mu_f|\mathbf{F}_{ab,n}| \end{cases} \tag{21}$$

The tangential relative velocity ($\mathbf{v}_{ab,t}$) and tangential unit vector ($\mathbf{t}_{ab}$) are defined as

$$\mathbf{v}_{ab,t} = \mathbf{v}_{ab} - \mathbf{v}_{ab,n} \qquad \mathbf{t}_{ab} = \frac{\mathbf{v}_{ab,t}}{|\mathbf{v}_{ab,t}|}$$

The tangential displacement, used in the tangential component of the contact force, is calculated via

$$\delta_t = \begin{cases} \delta_{t_0}\mathbf{H} + \int_{t_0}^{t} \mathbf{v}_{ab,t}dt & \text{if } |\mathbf{F}_{ab,t}| \leq \mu_f|\mathbf{F}_{ab,n}| \\ \frac{\mu_f}{k_t}|\mathbf{F}_{ab,n}|\mathbf{t}_{ab} & \text{if } |\mathbf{F}_{ab,t}| > \mu_f|\mathbf{F}_{ab,n}| \end{cases} \tag{22}$$

wherein the rotation matrix $\mathbf{H}$ provided by

$$\mathbf{H} = \begin{bmatrix} qh_x^2 + c & qh_xh_y - sh_z & qh_xh_z + sh_y \\ qh_xh_y + sh_z & qh_y^2 + c & qh_yh_z - sh_x \\ qh_xh_z - sh_y & qh_yh_z + sh_x & qh_z^2 + c \end{bmatrix} \tag{23}$$

where **h**, c, s, and q are defined as

$$\mathbf{h} = \frac{\mathbf{n}_{ab} \times \mathbf{n}_{0,ab}}{|\mathbf{n}_{ab} \times \mathbf{n}_{0,ab}|}, \qquad c = \cos\phi, \qquad s = \sin\phi, \qquad q = 1 - c$$

and

$$\phi = \arcsin(|\mathbf{n}_{ab} \times \mathbf{n}_{0,ab}|)$$

The tangential damping coefficient component of the spring–dashpot system is provided by Equation (24), where e_t is the tangential coefficient of restitution.

$$\eta_t = \begin{cases} \frac{-2\ln e_t \sqrt{\frac{2}{7} m_{\text{eff}} k_t}}{\sqrt{\pi^2 + \ln^2 e_t}} & \text{if } e_t \neq 0 \\ 2\sqrt{\frac{2}{7} m_{\text{eff}} k_t} & \text{if } e_t = 0 \end{cases} \tag{24}$$

In order to solve the particle motion and position, the differential equations require a certain time step, which depends on the duration of the contact. The time step for Discrete Element Model can be calculated by

$$\Delta t = \frac{1}{K_n} t_{\text{contact},n} = \frac{1}{K_n} \sqrt{\frac{m_{\text{eff}}(\pi^2 + \ln^2 e_n)}{k_n}} \tag{25}$$

where K_N is the minimum number of time steps during one contact. Previous experience with this code suggested to use a minimum of five time steps during one contact and to employ a normal range between 15 and 50 steps [25].

Since the contact force has normal and tangential components in the DEM model used, it is necessary to guarantee

$$t_{\text{contact},n} = t_{\text{contact},t} \tag{26}$$

which leads to

$$\sqrt{\frac{m_{\text{eff}}(\pi^2 + \ln^2 e_n)}{k_n}} = \sqrt{\frac{\frac{2}{7} m_{\text{eff}}(\pi^2 + \ln^2 e_t)}{k_t}} \tag{27}$$

In the case of equally normal and tangential restitution coefficients ($e_n = e_t$), the relation between the normal and tangential spring stiffness becomes

$$\frac{k_t}{k_n} = \frac{\frac{2}{7} m_{\text{eff}}}{m_{\text{eff}}} = \frac{2}{7} \tag{28}$$

Furthermore, it is suggested to ensure a maximum overlap that does not exceed 1% of the particle diameter [31]. The maximum overlap can be calculated via

$$\delta_{max} = \frac{v_0}{\Omega_0} \exp\left[-\frac{\Psi}{\Omega} \arcsin\left(\frac{\Omega}{\Omega_0}\right)\right] \tag{29}$$

where v_0 is the initial velocity, $\Omega_0 = \sqrt{\frac{k_n}{m_{\text{eff}}}}$, $\Omega = \sqrt{\Omega_0^2 - \Psi^2}$, and $\Psi = \frac{\eta_n}{2m_{\text{eff}}}$. Aside from the restitution and friction coefficients, the spring stiffness is also a numerical parameter that needs to be determined. However, this parameter is usually employed for the adjustment of the time step and maximum allowed overlap. For the simulations in this study, the spring stiffness was chosen sufficiently high so that it does not affect the results.

2.1.2. Inter-Particle Forces

Inter-particle forces can originate from multiple sources, including liquid bridging, sintering, and Van der Waals (VDW) forces. The last one is generally accepted as the dominant cohesive force in gas-fluidized beds [32].

In order to calculate the VDW forces between particles a and b, it is common to use the Hamaker expression [33–35]. Alternatively, when the primary goal is to assess the influence of inter-particle forces, the value is often expressed as a multiple factor of the gravitational force ($F_{vdw} = n^*F_g$). This study adopts the latter approach.

2.1.3. Drag Force

The gas–particle drag, or momentum exchange, is captured via accurate correlations in the CFD–DEM code. One of the most widely used correlations for dense gas–particle interactions is proposed by Gidaspow [36].

This correlation switches between the Ergun [37] equation for pressure drop in dense packed beds and the Wen and Yu [38] correlation for the terminal velocity of sedimentary spherical particles depending on the local porosity.

$$\beta_{\text{Gidaspow}} = \begin{cases} \frac{3}{4} C_D \frac{\rho_g \epsilon_g (1-\epsilon_g) |\mathbf{u}_g - \mathbf{v}_a|}{d_p} \epsilon_g^{-2.65} & \epsilon_g \geq 0.8 \\ 150 \frac{(1-\epsilon_g)^2 \mu_g}{\epsilon_g d_p^2} + 1.75 \frac{\rho_g (1-\epsilon_g) |\mathbf{u}_g - \mathbf{v}_a|}{d_p} & \epsilon_g < 0.8 \end{cases} \tag{30}$$

The drag coefficient C_D is calculated via Equation (31), which is dependent on the particle Reynolds number.

$$C_D = \begin{cases} \frac{24}{\text{Re}_p} \left(1 + 0.15 \text{Re}_p^{0.687}\right) & Re_p < 1000 \\ 0.44 & \text{Re}_p \geq 1000 \end{cases} \tag{31}$$

2.2. Gas Phase

In the CFD–DEM model, the gas phase is described by a compressible continuity Equation (1) and the volume-averaged Navier–Stokes momentum Equation (2). The total mass conservation is provided by Equation (1) where ρ_g is the gas density, ϵ_g is the local porosity, and $\mathbf{u}_g$ the gas velocity. The density of the gas phase is calculated via the equation of state for an ideal gas:

$$\rho_g = \frac{M}{RT_g} P_g \tag{32}$$

R is the ideal gas constant (8.314 J mol^{-1} K^{-1}), T_g the temperature of the gas phase in K, and M the total molecular weight of the gas phase. The momentum conservation equation is provided by Equation (2), where P_g is the gas phase pressure, $\mathbf{S}_p$ the source term that accounts for the momentum exchange between the gas and particle phases, τ_g is the gas phase stress tensor, and $\mathbf{g}$ is the gravitational acceleration. Newtonian behavior is assumed, which will lead to the stress tensor presented in Equation (3), where μ_g is the gas phase shear viscosity, $\mathbf{I}$ the unit tensor, and λ_g the gas phase bulk viscosity, which can be set to zero following Bird et al. [39]. The interface momentum exchange between the gas and particle phases is computed via Equation (4). Here, V represents the volume of the staggered cell, $V_{p,a}$ is the volume of particle a, and β is the interface momentum exchange coefficient, which can be calculated via a drag force closure shown in Equation (30). D is the distribution function that distributes the calculated momentum exchange to the Eulerian grid based on a volume weighing technique; see Tan et al. [40].

In order to solve the gas phase equations numerically, the domain is divided into a number of rectangular Eulerian grid cells and the equations are discretized via a standard finite difference technique. The cells are labeled via i, j, and k, which are located at the cell

centers regarding the x-, y-, and z-directions, respectively. The velocities are defined at the cell faces, whereas the scalar variables are located at the cell centers.

The total continuity and volume-averaged Navier–Stokes equations are solved via the adaptive SIMPLE algorithm, where pressure correction is utilized following the work of Kuipers et al. [41] in such a way that the discretized form of the total continuity equation is satisfied.

3. Set-Up for the CFD–DEM Simulations

The simulations are split into two main parts: the first set of simulations considers a parameter study on the particle collisional properties, in particular studying the effect on the minimum fluidization velocity (U_{mf}) and fluidized bed hydrodynamics (bed porosity, solid circulation, and bubble behavior). By keeping the gas properties (density and viscosity) constant, this part mimics a temperature response of the system when only particle collisional properties are temperature-dependent. The second part of the investigation evaluates the whole effect of the temperature on fluidization, i.e., when both gas and particle collision properties are affected. Here too, the interest involves the minimum fluidization velocity and the fluidization hydrodynamics. This section also discusses when inter-particle forces are required to fully capture the effect of temperature on fluidization.

Table 2 presents the main settings of the parameter study on the particle collisional properties. These simulations are based on the work of Laverman [23], in particular concerning the chosen geometry and particle size and density based on polyolefin particles. Collision properties of particles are difficult to measure and require a devoted experimental set-up. For this sensitivity study, we aim to cover an entire parameter space for e_n, e_t, and μ_f. To limit the number of combinations, we only change one of these parameters while keeping the other two constant. The employed values are also indicated in Table 2.

Table 2. Simulation settings for the parametric investigation of particle collision properties on minimum fluidization velocity and bed hydrodynamic studies.

Parameter	Minimum Fluidization	Fluidization Hydrodynamics
Width x-direction [m]	0.0206	0.06696
Depth y-direction [m]	0.0206	0.0103
Height z-direction [m]	0.09727	0.2163
Grid cells (x,y,z)	8, 8, 36	26, 4, 84
Number of particles [-]	12,000	45,500
	General parameters	
Particle diameter [m]	0.00103	
Particle density [kg m^{-3}]	800	
Normal restitution coefficient e_n [-]	1.0, 0.98, 0.8, 0.6, 0.3, 0.1	($e_t = 1.0$; $\mu_f = 0.0$)
Tangential restitution coefficient e_t [-]	1.0, 0.9, 0.6, 0.3	($e_n = 1.0$; $\mu_f = 0.1$)
Frictional coefficient μ_f [-]	0.0, 0.01, 0.1, 0.3, 0.6, 0.9	($e_n = 1.0$; $e_t = 1.0$)
Normal spring stiffness [N m^{-1}]	750	
Tangential spring stiffness [N m^{-1}]	220	
Time step [s]	1×10^{-4}	

To determine the minimum fluidization velocity, the particles were fluidized for two seconds with a gas velocity high enough to observe an obvious bubbling behavior (0.4 m s^{-1}), after which they were left to settle down. Then, starting from this fixed bed situation, the gas velocity was increased slowly over the whole bottom plate until it reached 0.4 m s^{-1}. At this point, the system was fluidized for one second, after which the gas flow velocity was slowly decreased again to reach zero. This procedure is crucial for a proper analysis of the minimum fluidization velocity using pressure drop values. All the simulations on minimum fluidization were performed at room temperature with nitrogen

as fluidization gas. Both increases and decreases in gas velocity simulations were performed. Relative to the values of the minimum fluidization velocities, simulations for bubbling behavior were performed at the excess gas velocity of 0.32 m s^{-1}.

As stated before, in the second part of this research, not only will the particle collision properties change with temperature but also the gas properties. The settings for this second set of simulations are provided in Table 3. In this case, they were performed with glass-like particle properties in order to reproduce the experimental work of Campos Velarde [8]. To match the predicted minimum fluidization velocity with the experimental data, the collisional particle properties were tuned using the patterns found in the parametric study that is presented before in the results section.

Table 3. Simulation parameters for the investigation of the combined effect of temperature on gas and particle collision properties.

Parameter	Minimum Fluidization	Fluidization Hydrodynamics
Width x-direction [m]	0.01	0.0325
Depth y-direction [m]	0.01	0.005
Height z-direction [m]	0.042	0.105
Grid cells (x,y,z)	8, 8, 36	26, 4, 84
Number of particles [-]	12,000	45,500
Particle diameter [m]	0.0005	
Particle density [kg m^{-3}]	2500	
Temperature [K]	293.15, 373.15, 473.15, 573.15	
Gas viscosity 1×10^{-5} [Pa s]	1.76, 2.12, 2.51, 2.86	
Gas density [kg m^{-3}]	1.165, 0.915, 0.722, 0.596	
Normal spring stiffness [N m^{-1}]	6620	
Tangential spring stiffness [N m^{-1}]	1892	
Hamaker constant ($\mathbf{F}_{\mathrm{VDW}} = 1 \times \mathbf{F}_{\mathrm{gravity}}$) [J]	1.73×10^{-19}	
Hamaker constant ($\mathbf{F}_{\mathrm{VDW}} = 2 \times \mathbf{F}_{\mathrm{gravity}}$) [J]	3.47×10^{-19}	
Inter-particle cut-off [m]	1.5×10^{-9}	
Time step [s]	1×10^{-5}	

4. Results and Discussion

4.1. General Effect of Restitution and Friction Coefficients on Fluidization

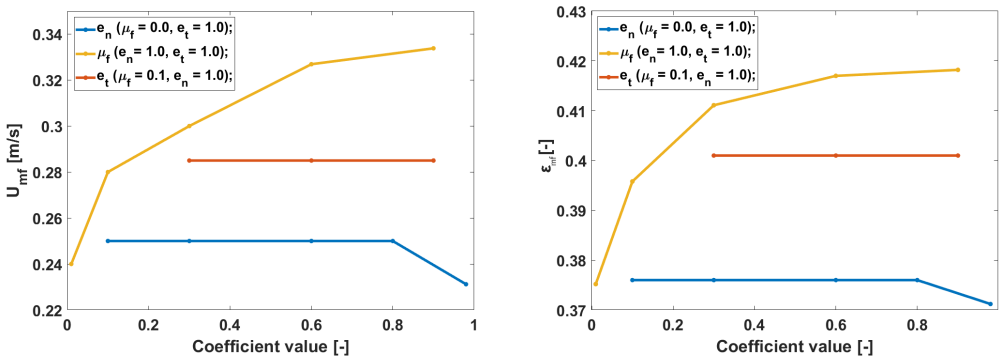
This section presents a parameter study on the effect of the restitution and friction coefficients on the hydrodynamics of the bed. The minimum fluidization velocity of the bed will be investigated. Then, an excess velocity is introduced to the bed and the effect of the collisional parameters on a single injected bubble and the bubbling fluidization regime will be discussed (see simulation conditions in Table 2).

4.1.1. Minimum Fluidization Velocity

The pressure drop over the bed is recorded during the increase and decrease in the superficial gas velocity. The minimum fluidization velocity can then be determined from the pressure drop versus gas velocity graphs, as explained by Kunii et al. [42]; when the bed is in a packed or expanded state, the pressure drop responds linearly to the gas velocity. When the bed is in a fluidized (bubbling) state, the pressure drop levels off towards a more or less constant value. The intercept between these two trends indicates the minimum fluidization velocity.

The results for the minimum fluidization velocities for the collisional parameters are presented in Figure 1a. An initial investigation was performed for different values of normal restitution coefficient (e_n) for the values listed in Table 2. Similar to the outcomes reported by Laverman [23], the change in the normal restitution coefficient shows a negligible effect on the fluidization velocity, even for the smaller values of the coefficient. Only a slight decrease in the minimum fluidization velocity was observed with the largest values of

normal restitution coefficient ($e_n > 0.98$). This combination of parameter values is very close to ideal collisions (near fully elastic collisions with a very low loss of energy). The energy dissipation is not large enough for porosity differences to form and stabilize, which is a requirement for bubbles to form. Instead, in the current state, particles spread evenly through the assigned space, and the bed simply only expands under the influence of drag and gravity.



(**a**) Minimum fluidization velocity. (**b**) Minimum fluidization porosity.

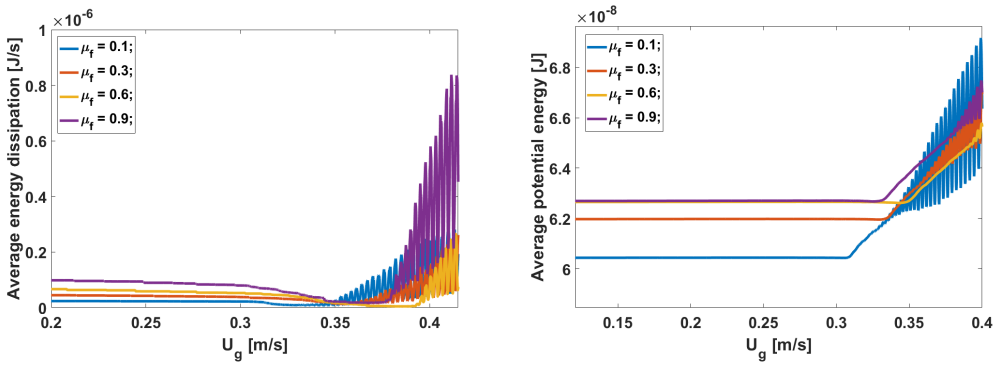
Figure 1. Minimum fluidization conditions as a function of selected particle collisional parameters.

Similar to the normal restitution coefficient, the tangential restitution coefficient also did not show an effect on the minimum fluidization velocity. It is important to mention that the friction coefficient has not been set to the ideal value of 0.0 but rather to 0.1 since the tangential collision itself (Equation (21)) only has an effect if the friction coefficient is nonzero. This small influence of e_t on the minimum fluidization velocity was also found in Laverman [23].

The last collisional parameter, the friction coefficient, shows an increase in the minimum fluidization velocity when its value is increased. This behavior can be attributed to the packing of particles within the bed. As the friction between particles increases, it suggests that the particles are positioned closer together, leading to overlap between them. The manifestation of this can be observed in the dissipated and potential energy of the packed bed, before the fluidization onset, as presented in Figure 2 (computed with Equations (33) and (34)); it is shown that a packed bed with a higher friction coefficient has a higher average potential energy.

$$E_{\text{dsp}} = \int \sum_{a}^{N_{part}} \sum_{b} (\mathbf{F}_{ab,n} + \mathbf{F}_{ab,t}) \cdot \mathbf{v}_{ab} dt \quad \text{where} \quad b > a \ \text{ and } \ b \in \text{contact list of a} \tag{33}$$

$$E_{\text{pot}} = \sum_{a}^{N_{part}} m_a (g\, h_a) \tag{34}$$



(**a**) (**b**)

Figure 2. Energy states of the system affected by changes in friction coefficient. (**a**) Average energy dissipation due to friction contact—sliding. (**b**) Average potential energy of the system.

In conclusion, the effect of the normal and tangential restitution coefficients on the particle bed packing is negligible compared to the friction coefficient. Figure 1b presents the effect of the friction and restitution coefficients on the porosity of the packed bed, which explains the influence on the minimum fluidization velocity.

4.1.2. Single-Bubble Injection

In order to better understand the hydrodynamics during the bubbling fluidization, this section investigates how the normal and tangential restitution coefficients and friction coefficient influence a single rising bubble injected into a bed under minimum fluidization conditions. The bed was initialized at a gas flow of $U = 0.6\ \mathrm{m\,s^{-1}}$, after which the gas flow was reduced to U_{mf} and, after one second, a bubble was injected by setting the gas velocity through the central cells to $5.8\ \mathrm{m\,s^{-1}}$ for 0.1 s.

Again, the settings from Table 2 were used to scan the parameter space. Figure 3 presents snapshots of the simulations for different normal restitution coefficients. It can be observed visually that a value of $e_n = 0.8$ yields a slightly smaller bubble compared to the other cases. This behavior, explained by high values of the normal restitution coefficient, hinders bubble formation and was also found in Hoomans et al. [24] using $e_n = 1.0$. In Figure 4a, the probability density function of the porosity, averaged over the entire bubble life time, is presented. Although for $e_n = 0.8$ the more intense raining of particles through the bubble roof results in a slightly different value of the porosity profile, the other values for the normal restitution coefficient do not show the change in bubble size. The performed simulations with semi-ideal conditions show that the normal restitution coefficient might have an effect on bubble behavior for $e_n > 0.8$, while for the lower values the effects fades away.

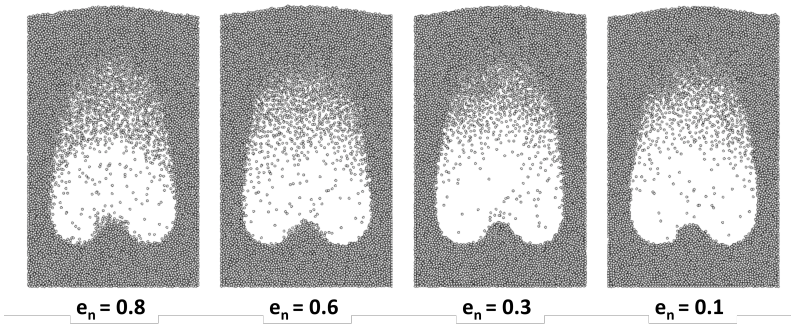
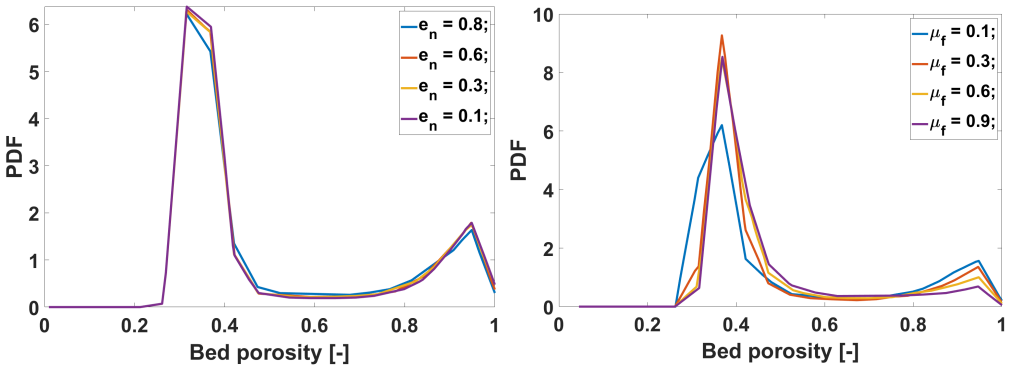


Figure 3. Screenshots of single-bubble injection for different normal restitution coefficients.



(**a**) PDF—ε (e_n). (**b**) PDF—ε (μ_f).

Figure 4. Probability density function of the porosity for a single-bubble injection at different values of normal restitution coefficient and friction coefficient.

The results with a changing friction coefficient show much more noticeable differences in the time-averaged porosity profile. From the snapshots of the bubble injection in Figure 5, it can be observed that, for higher friction coefficients, the bubble size will decrease. In the probability density function of the porosity, Figure 4b presents a clear indication that the bubble size is smaller.

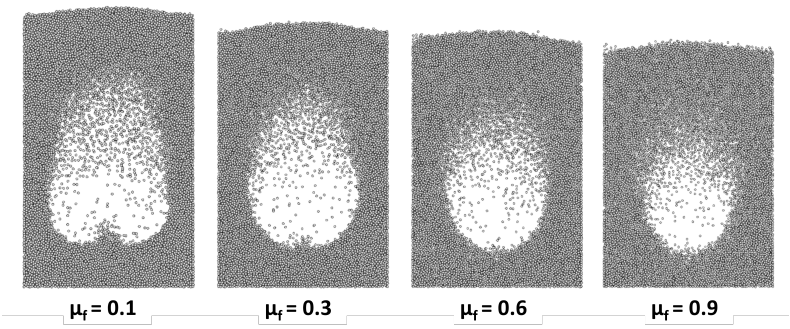


Figure 5. Screenshots of single-bubble injection for different friction coefficients.

The change in tangential restitution coefficient had no significant effect on the bubble properties. Also, no significant change in the probability density function of porosity has been observed.

4.1.3. Bubbling Fluidization

In this section, the general influence of the particle collision properties on the bubbling fluidization hydrodynamics is explored. The particles in this section were fluidized with an excess velocity of 0.32 m s^{-1} compared to the calculated minimum fluidization velocity. The other parameters of the numerical set-up are presented in Table 2. In addition to those, one case is presented with fully ideal conditions, where the normal and tangential restitution coefficients were set to 1.0 while the value for the friction coefficient is 0.0.

The total fluidization time was 30 s in order to achieve good time-averaged values. In this part of the investigation, isolation of the effect of the specific particle property will be presented by changing one, while others have ideal collision values ($e_n = 1.0, e_t = 1.0, \mu_f = 0.0$).

The time-averaged particle phase velocity fields are provided in Figure 6. Similar to the reported results by Laverman et al. [7], the circulation pattern shows a solid up-flow in the middle of the bed and down-flow along the side walls. The ideal case shows no occurrence of bubbles, but the circulation of the particles was present nonetheless but much less pronounced. A slight modification of the normal restitution coefficient to $e_n = 0.98$ also showed this behavior; bubbles do not develop, and this causes a low circulation intensity. A further reduction in the normal restitution coefficient initiates bubbling fluidization. This lack of bubbling fluidization with collision parameters so close to the ideal conditions was also found in 2D simulations by Hoomans [43]. The solid circulation intensity becomes stronger with higher collisional energy dissipation, but the largest change in velocity occurs between the values of 1.0 and 0.8. At values below $e_n = 0.6$, an additional effect on the solid circulation profiles can hardly be observed. In order to answer why this is occurring, an investigation on the bubble size and particle velocity and porosity in the bed is necessary.

The probability distribution function of the time-averaged bed porosity is presented in Figure 7a. The ideal case shows a single peak for a homogeneously expanded bed, while, for $e_n = 0.98$, the porosity distribution already starts to widen, even though there are no visible bubbles. A more distinct bubble phase (typically, bubbles are defined as regions with $\varepsilon \geq 0.8$) becomes visible as the restitution coefficient is decreased, analogous to the observations for the single-bubble injection. For values $e_n \leq 0.8$, no significant porosity changes can be observed.

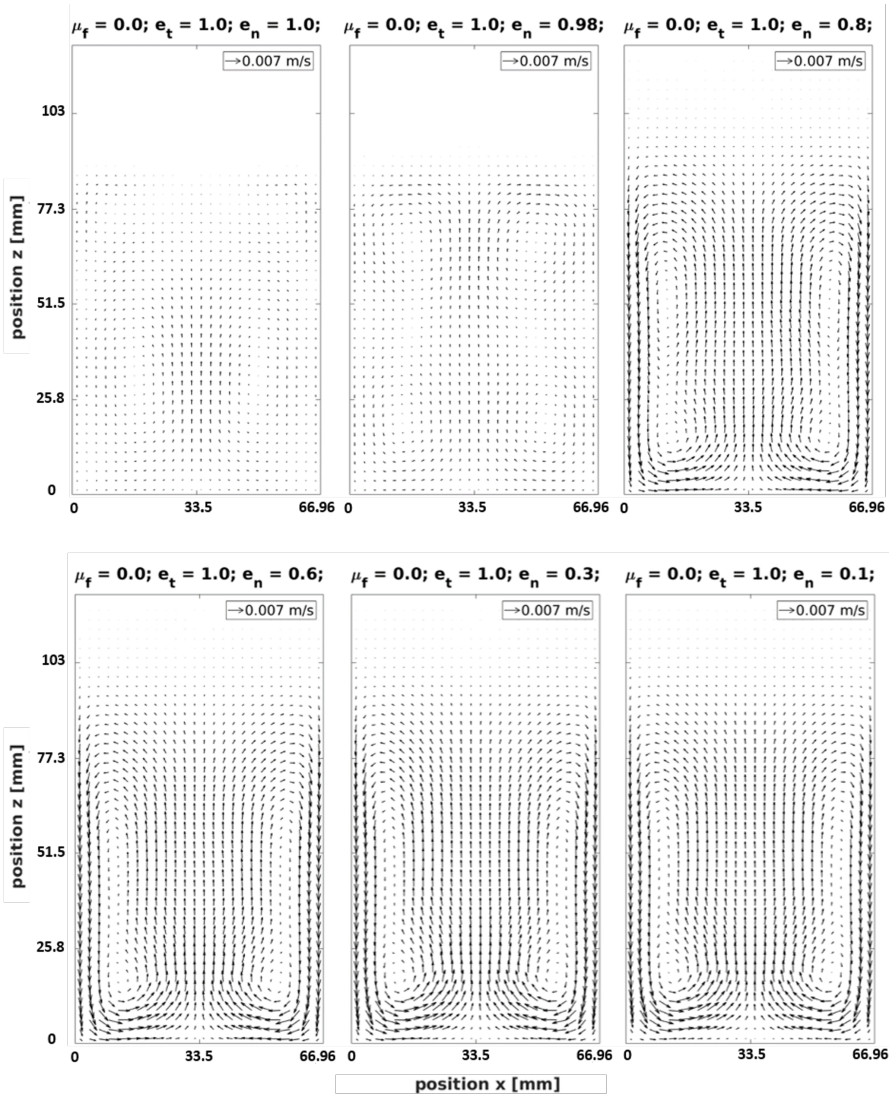
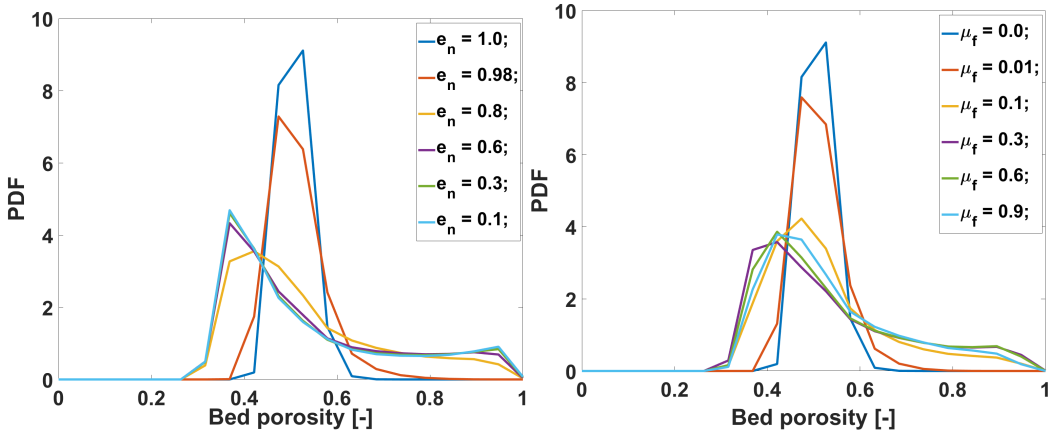


Figure 6. Time-averaged solid circulation patterns for different normal restitution coefficients.

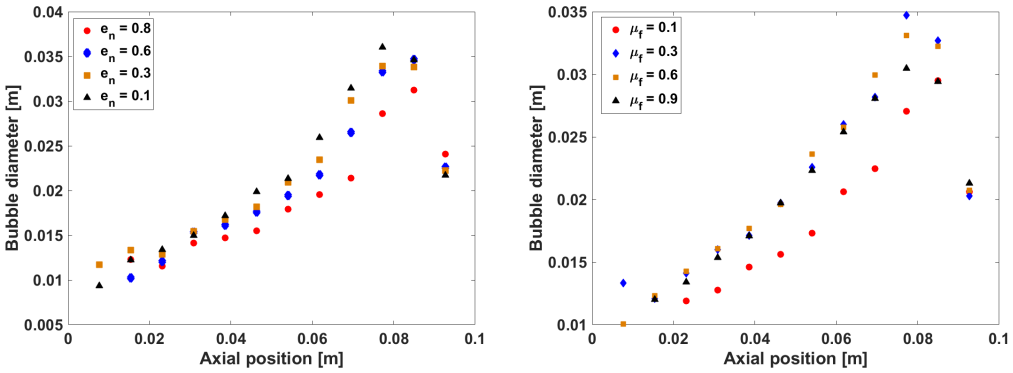


(**a**) PDF—ε (e_n). (**b**) PDF—ε (μ_f).

Figure 7. Probability density function of the porosity for the fluidization conditions presented for different values of normal restitution coefficient and friction coefficient.

The bubbles have been characterized using Digital Image Analysis, similarly to Laverman et al. [7]. Figure 8a presents the bubble size as a function of the axial position, which indicates that bubbles grow along the height of the system. The growth is more apparent for smaller normal restitution coefficients. The higher collisional energy dissipation causes

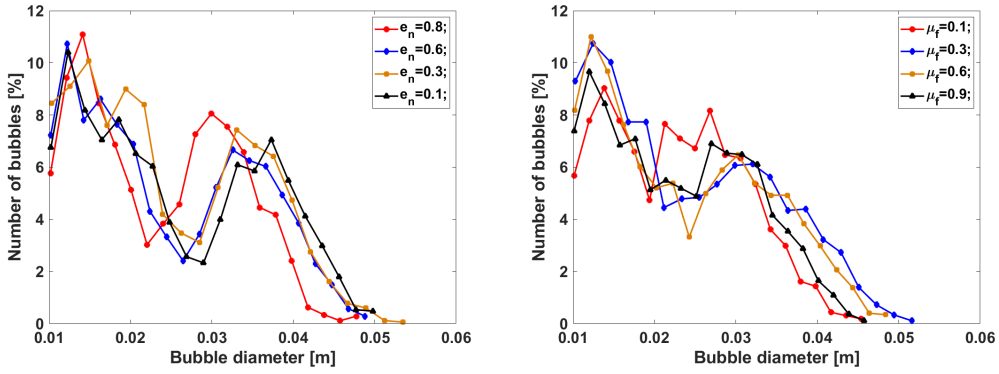
fewer particles to migrate to the bubble interior, while the excess gas flows towards the highest porosity zones, inflating the bubble even further.



(**a**) Bubble diameter over height (e_n). (**b**) Bubble diameter over height (μ_f).

Figure 8. Bubble diameter over height for the fluidization conditions presented for different values of normal restitution coefficient and friction coefficient.

The average porosity over the different bed heights showed that a smaller normal restitution coefficient will result in higher porosity values in the middle of the bed and smaller values (more densely packed particles) along the side walls, indeed indicating larger bubbles through the center. This is also backed up with the shift to larger bubbles as e_n decreases in the bubble size distributions in Figure 9a. On the other hand, the average particle velocity increased in the middle of the bed, with slower movement on the sides. These two counteracting effects cause the lack of overall change in the particle velocity shown in Figure 6.



(**a**) (**b**)

Figure 9. Number of bubbles depending on their size for the fluidization conditions presented for different values of normal restitution coefficient and friction coefficient. (**a**) Number of bubbles depending on their size (e_n). (**b**) Number of bubbles depending on their size (μ_f).

The time-averaged solid circulation patterns for varying friction coefficients are presented in Figure 10. Similar to the case where $e_n = 0.98$, here, the value of $\mu_f = 0.01$ provides results that are similar to fully ideal collisions since the energy dissipated by a collision is very small, which prevents the formation of bubbles. For sufficiently high values of the friction coefficient, in simulations where $\mu_f > 0.1$, bubble formation starts and the solid circulation intensifies. A trend-breaking effect is caused by a further increase in the friction coefficient; from $\mu_f = 0.3$, a slight reduction in the particle circulation is observed, which can be better explained by considering the bubble characteristics.

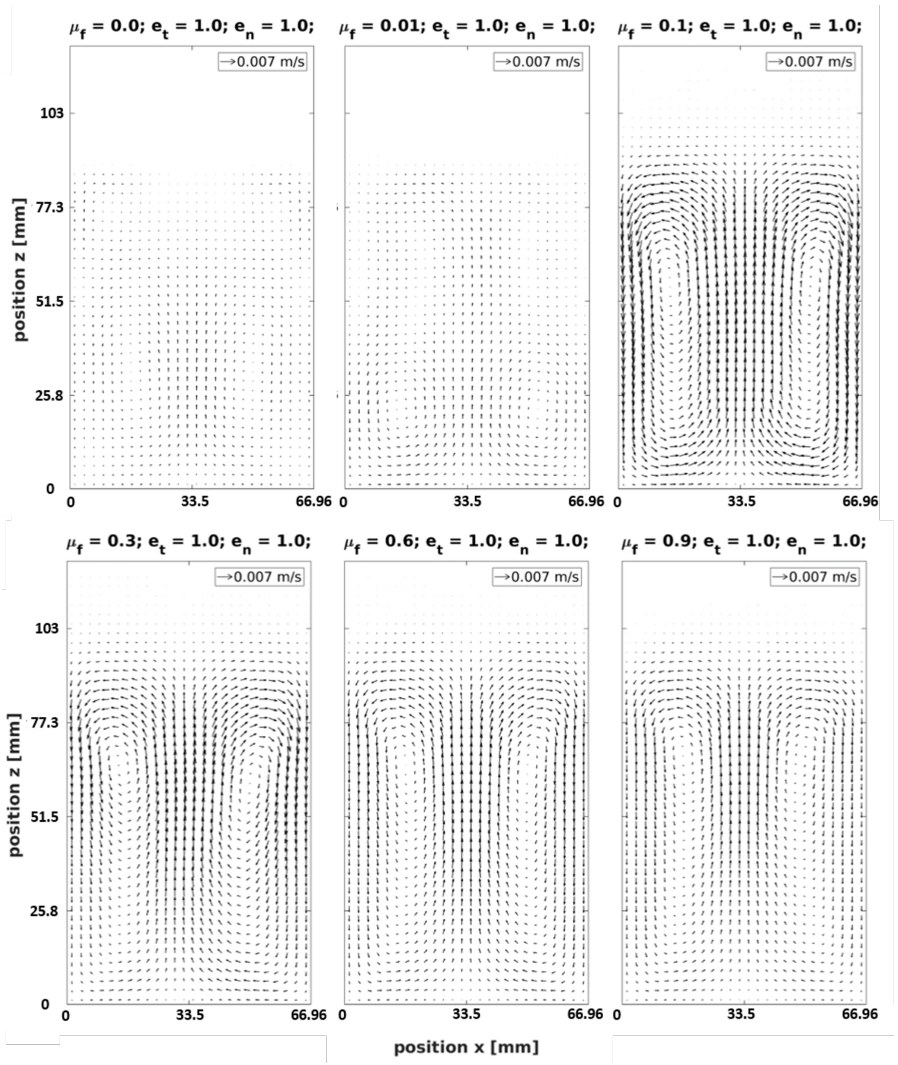


Figure 10. Time-averaged solid circulation patterns for different friction coefficients.

The bubble size as a function of height for different values of the particle friction coefficient is shown in Figure 8b. Freely bubbling behavior was only observed for $\mu_f \geq 0.1$, and, in every case, the bubble size grows with height. For the lowest friction case that develops bubbles, $\mu_f = 0.1$, the growth is somewhat less pronounced than for the other cases ($\mu_f \geq 0.3$) under investigation, where the bubbles grow at a similar rate. From these results, an important conclusion can be reached that some energy dissipation due to friction is required to form bubbles, which in turn induces the main circulation in the solid phase. However, at higher frictional rates, the circulation motion decreases again as the energy dissipation due to friction grows beyond the energy induced by the rising bubbles. This causes the circulation intensity to reduce. Hence, if the temperature would cause a change in the solid friction (due to its effect on the collision parameters), the response of the solid circulation would be non-linear.

The time-averaged particle velocity field presented in Figure 10 reduces with the increase in the friction coefficient. Bubble fluidization starts with $\mu_f > 0.1$; the bubble size distribution in Figure 9b for the value of $\mu_f > 0.1$ showed that smaller and more uniform-sized bubbles appear. As the value of the friction coefficient is increased, the bubble size distribution becomes bimodal. With the increase in the friction coefficient, the bubble size reduces, as presented in both size distributions over the bed height and in general occurrences of the bubbles. Figure 9b shows a number density function of bubble

sizes, which indicates that the maximum size of the bubble decreases for higher values of the friction coefficient.

Another notable finding is the correspondence in bubble characterization between predictions for bubbling fluidization and single-bubble injection. In both cases, the changes in the normal restitution coefficient have a minor effect on the bubble size (compare Figures 4a and 8a). However, the slight decrease in bubble size with increasing restitution coefficient, as shown in Figure 3, is also observed in Figure 8a. Changes in the friction coefficient, as shown in Figures 4b and 5, have a more significant impact, particularly when increasing from $\mu = 0.1$ to $\mu = 0.3$. This effect is further confirmed in Figure 8b, where the friction coefficient has a noticeable influence.

An investigation on the tangential restitution coefficient has also been performed regarding the cases presented in Table 2. Here too, the results showed no change for the average particle velocity field, as can be seen in Figure 11. The analysis showed that decreasing the tangential restitution coefficient did not have a significant influence on the particle velocity, porosity distribution, and bubble size. In Figures 12 and 13, supporting behavior for these statements is demonstrated. Similarly, Hoomans [43] found that only by using unrealistically high friction coefficient values and hence promoting sticking collisions was it possible to observe an effect of the tangential restitution coefficient on the fluidization behavior.

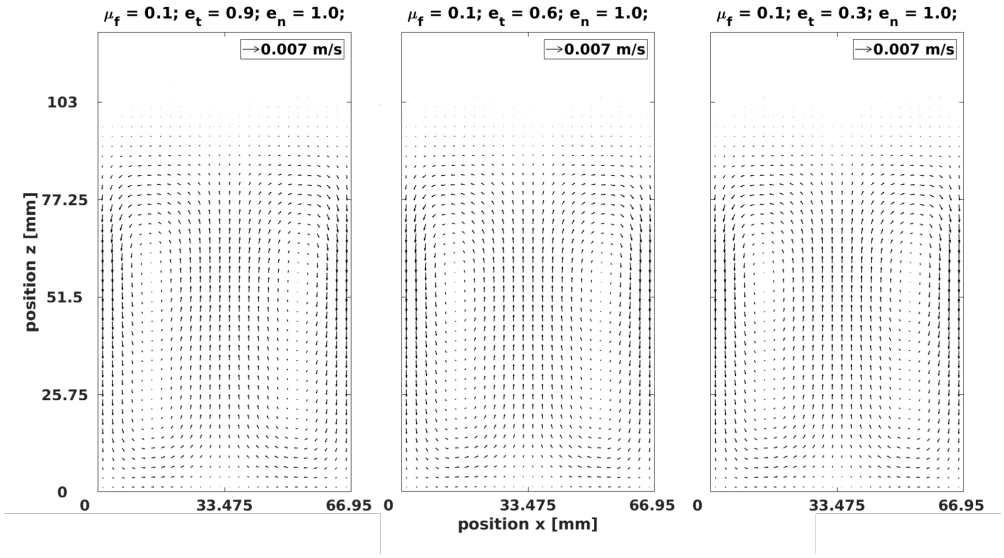
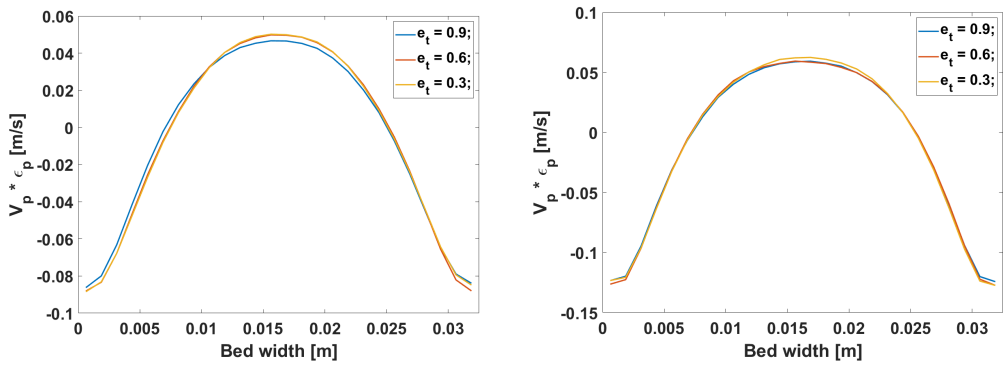
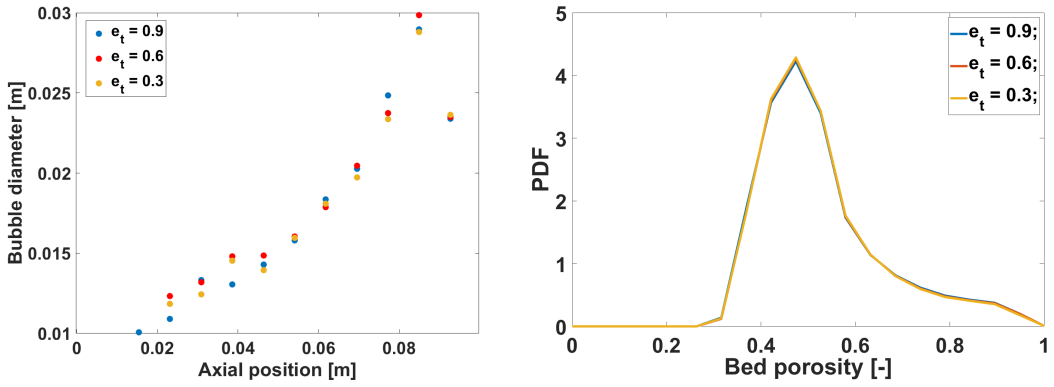


Figure 11. Time-averaged solid circulation patterns for different tangential restitution coefficients.



(**a**) Quarter height of the bed. (**b**) Middle height of the bed.

Figure 12. Particle velocity at different heights of the bed for different tangential restitution coefficients.



(**a**) (**b**)

Figure 13. Bubble size and porosity distributions for the cases with different tangential restitution coefficients. (**a**) Bubble diameter over height for cases with different e_t. (**b**) PDF of porosity for cases with different e_t.

4.2. Fluidization of Glass Particles at Different Temperatures

The experimental results by Campos Velarde [8] have shown that the role of the temperature on the fluidization regime is not as small as is commonly assumed. However, as the temperature also affects the gas properties, the particle collisional properties (viz. restitution and friction coefficients) and inter-particle forces are challenging to untangle experimentally. Therefore, this part of the study will present the numerical equivalents of these experiments in order to clarify the role of the particle properties and the inter-particle interactions as Van der Waals forces (see simulation conditions in Table 3).

4.2.1. Experimental Parameters

To facilitate the upcoming discussion, this section outlines the settings of the three main experimental campaigns by Campos Velarde [8]. The results from these campaigns will be presented in the following sections in comparison with the numerical simulation results from the current study.

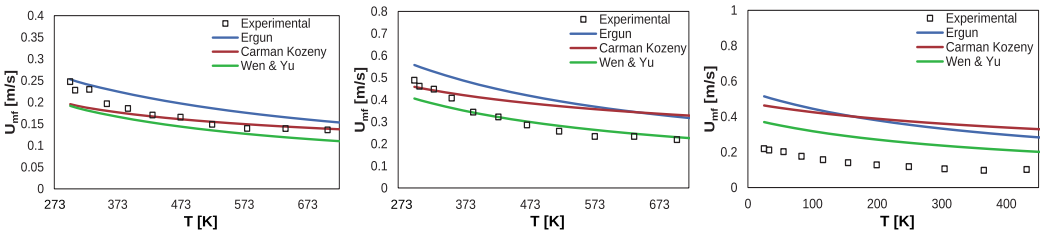
Minimum fluidization velocity The minimum fluidization velocity has been measured using nitrogen, hydrogen, and helium by pressure-drop measurements, as a function of temperature, using 528 µm glass beads.

Constant gas properties at different temperatures In order to exclude the influence of the gas properties due to changing temperature, two different gases were composed that have a similar density (0.712 kg m^{-3}) and viscosity (25.07 $\times$ 10^{-6} Pa $\cdot$ s) at different temperatures, viz. nitrogen at 473 K and a mixture of helium and argon (0.58:0.42) at 323 K, using glass beads of 400–600 µm.

Bubbling fluidization at different temperatures Bubbling fluidization was performed using nitrogen at 293, 373, 473, and 573 K, again using 400–600 µm glass beads.

4.2.2. Minimum Fluidization Velocity of Glass Particles

Experimentally, a consistent decline in the minimum fluidization velocity with increasing temperature has been observed, regardless of the type of gas used, as shown in Figure 14. A set of simulations were performed in order to find a suitable combination of particle collisional properties in an attempt to determine similar values of the minimum fluidization velocity.



(**a**) Nitrogen (**b**) Hydrogen (**c**) Helium

Figure 14. Minimum fluidization velocity as a function of temperature of 528 µm glass beads fluidized with different gases compared to literature correlations from Ergun, Wen and Yu, and Carman-Kozeny [37,38,44–46]. Experimental data as reported by Campos Velarde [8].

In Section 4.1.1, it was observed that a decrease in the normal restitution coefficient has a negligible effect on the minimum fluidization velocity, whereas increasing the friction coefficient increases the minimum fluidization velocity. However, changing the gas properties with temperature should at least partially have the desired effect of reducing the minimum fluidization velocity, as was demonstrated in previous experimental works [2–4,47].

In order to reproduce the U_{mf} experimental results at different temperatures using nitrogen gas, initially only the gas density and viscosity were adjusted (see Table 3), while the particle properties were fixed at $e_n = 0.9$, $e_t = 0.33$, and $\mu_f = 0.1$ to represent glass bead behavior. The results in Figure 15 demonstrate an under-prediction of U_{mf} for the higher temperatures, indicating that an additional temperature-dependent effect must be included. Since data on the change in particle properties with temperature are not unambiguously available, the values were manually tailored to match U_{mf} to the experimental results.

Figure 15 additionally illustrates the scenario in which both the gas characteristics were modified and the collisional characteristics were fitted. It becomes clear that, without adjusting the collisional properties, simulations at elevated temperatures will under-predict the minimum fluidization velocity, which can lead to severe deviations in the simulation of full-scale fluidized beds.

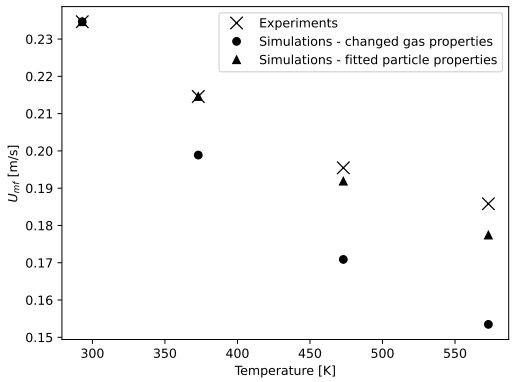


Figure 15. Minimum fluidization velocity simulated at different temperatures, changing the gas and particle properties, in comparison with experimental results.

Although all the parameters were considered for adjustment to match the experimental results, the results from Section 4.1.1 demonstrate that ultimately an increase in the particle friction coefficient would produce the largest influence. For each temperature, the friction coefficient was increased until it matched the experimental value. Tables 4 and 5 show that, for higher temperatures, the influence of the friction coefficient on the minimum fluidization velocity reaches a plateau. This velocity cannot be achieved only by tuning

the collisional parameters without increasing, e.g., the friction coefficient to some high and unrealistic values.

In order to prevent the friction coefficient rising beyond physically realistic values, and following the hypotheses of Campos Velarde [8], an additional influence will be introduced in the form of inter-particle forces. Specific inter-particle forces are the attractive Van der Waals forces that have a large or even dominant influence on the fluidization of the particles that are in the range of the Geldart A and Geldart C types; see [48]. However, it is often suggested that these forces could also have an influence on Geldart B type particles, as in the present case [4,6,8]. Knowing that the introduction of these forces will increase the minimum fluidization velocity, an additional influence of the VDW forces was created regarding the particles for the temperatures of 473 and 573 K, where the effect of the friction coefficient was found to plateau. For the simulation at 473 K and setting the van der Waals force equal to the force of gravity, it was shown to be sufficient to match the experimental data for the minimum fluidization condition, while, for the simulation at 573 K, the Van der Waals force equal to two times gravity was sufficient. The simulation parameters are provided in Table 3.

This modification enables matching the experimental U_{mf} results (see Table 5). With the addition of the VDW forces, the observed stickiness of the particles that was recorded after the fluidization at the higher temperatures in the experiments can be explained and described.

Minimum fluidization conditions at 323 K could be simulated by increasing only the friction coefficient, without any additional forces or conditions, which also explains that fluidization under normal ambient conditions does not require setting a force as exotic as the VDW force; this is only necessary for special cases (i.e., very fine particles or elevated temperature). The values gathered match the data from the experiments, and these simulations suggested an increase in the friction coefficient and in the strength of the van der Waals forces with temperature. It is believed that additional changes in the normal restitution coefficient could occur; however, this effect should be more easily detected under bubbling fluidization conditions and will be explored in the next section.

Table 4. Minimum fluidization velocity of glass particles for gas temperatures between 293 K and 373 K. The colors are meant to guide the eye for the combination of collision properties that, for a particular temperature, that resembles most closely the experimentally determined value, based on the value for u_{mf} printed in boldface.

e_n/$\mathbf{F}_{vdw}$	$e_n = 0.90$	$e_n = 0.90$	$e_n = 0.90$	$e_n = 0.90$	$e_n = 0.90$	$e_n = 0.90$	Experiment
μ_f	$\mu_f = 0.1$	$\mu_f = 0.12$	$\mu_f = 0.14$	$\mu_f = 0.16$	$\mu_f = 0.18$	$\mu_f = 0.22$	U_{mf}[m/s]
T = 293 K	**0.2345**						**0.235**
T = 323 K	0.1727	0.1730	**0.1732**	0.1776	0.1786		**0.1758**
T = 373 K	0.1986	0.1998	0.2016	0.2045	0.2085	**0.2144**	**0.2145**

Table 5. Minimum fluidization velocity of glass particles for gas temperatures between 473 K and 573 K. The colors are meant to guide the eye for the combination of collision properties that, for a particular temperature, that resembles most closely the experimentally determined value, based on the value for u_{mf} printed in boldface.

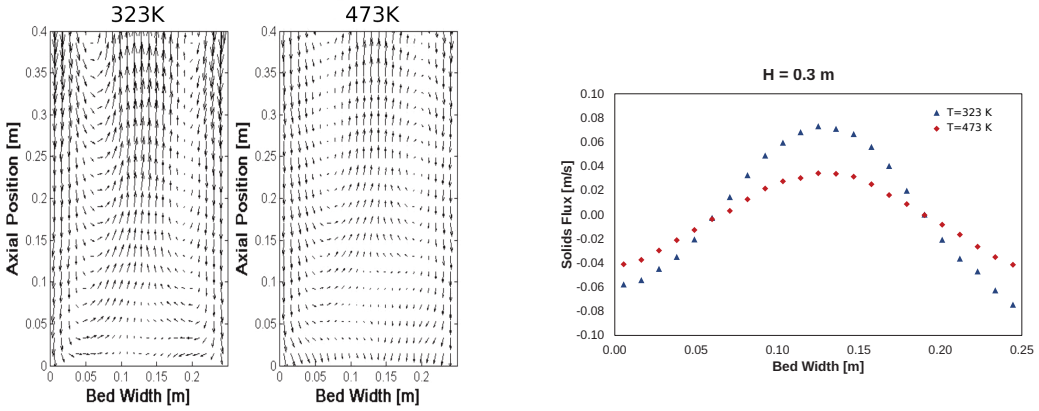
e_n/$\mathbf{F}_{vdw}$	$e_n = 0.90$	$e_n = 0.90$	$e_n = 0.90$; $\mathbf{F}_{vdw} = 1\mathbf{F}_g$	$e_n = 0.90$	$e_n = 0.90$	$e_n = 0.90$; $\mathbf{F}_{vdw} = 2\mathbf{F}_g$	$e_n = 0.90$	Experiment
μ_f	$\mu_f = 0.1$	$\mu_f = 0.3$	$\mu_f = 0.3$	$\mu_f = 0.32$	$\mu_f = 0.38$	$\mu_f = 0.38$	$\mu_f = 0.48$	U_{mf}[m/s]
T = 473 K	0.1707	0.1917	**0.1989**	0.1917				**0.1951**
T = 573 K	0.1531				0.1752	**0.1847**	0.1773	**0.1858**

4.2.3. Bubbling Fluidization Velocity of Glass Particles

In this section, the time-averaged solid circulation pattern profiles resulting from our simulations are compared to the experimental results. We distinguish two cases

(see Section 4.2.1): one employing two gas mixtures that have the same gas properties at different temperatures and another where nitrogen is the fluidizing agent at different temperatures. In all the simulations, the parameters were kept consistent with those in the experiments. The bubbling fluidization regime was achieved with an excess velocity of 0.32 m s^{-1} above the minimum fluidization velocity. In order to achieve good temporal averaging, simulations were performed for 30 s.

As for the first case, the minimum fluidization velocity was found to be different for the two gas compositions used: 0.1758 m s^{-1} using the helium and argon mixture and 0.1951 m s^{-1} for pure nitrogen. To facilitate a smooth experience of the upcoming discussion, we revisit the main experimental findings in Figure 16. Figure 16a shows a clear reduction in particle velocity at 473 K despite constant gas properties. This is confirmed with the flatter solid velocity profile at higher temperatures in Figure 16b.

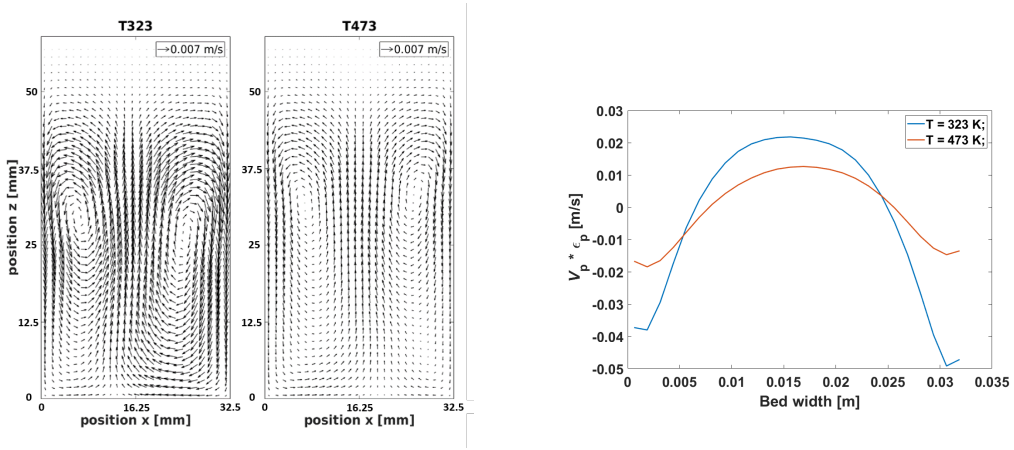


(**a**) Solid circulation patterns. (**b**) Particle velocity profiles at mid-height.

Figure 16. (**a**) Experimental behavior of 400–600 µm glass beads fluidized with nitrogen at 473 K and a He:Ar mixture at 323 K with the same excess velocity. (**b**) Time-averaged solid velocity profiles at H = 0.3 m; adapted from Campos Velarde [8].

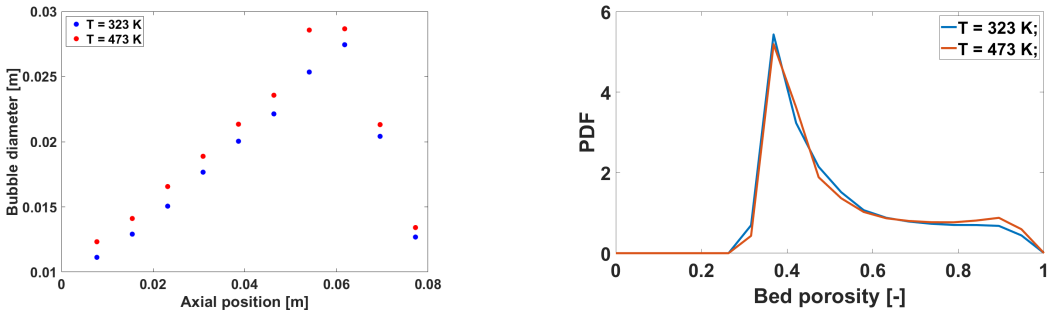
Figure 17a presents the results of the CFD–DEM simulations, indicating trends that are consistent with the experimental findings. This agreement highlights the critical role of the (fitted) increase in the particle friction coefficient in the particle circulation. Adjusting the friction coefficient is particularly important for accurate modeling of high-temperature conditions. Figure 17b illustrates that a higher friction coefficient reduces the solid circulation in the middle of the bed, while the circulation pattern remains qualitatively the same. Finally, Figure 17a shows some asymmetry in the circulation patterns, especially at low temperatures. This could indicate that, while the 30 s simulation time is sufficient to obtain meaningful results, small inaccuracies might persist. In Figure 18a, the bubble diameter along the column shows a slight increase with temperature. This observation aligns with the porosity distribution in Figure 18b, where lower temperatures correspond to a slightly wider porosity distribution.

The behavior observed in Figures 17 and 18 is consistent with the findings of the sensitivity analysis in Section 4.1.3. Specifically, an increase in the friction coefficient above 0.1 results in a reduction in particle velocity and an increase in bubble size.



(**a**) Solid circulation patterns. (**b**) Particle velocity profiles at mid-height.

Figure 17. (**a**) Time-averaged solid circulation patterns for two cases of same gas properties. (**b**) Particle velocity at the middle of the bed for the same gas properties at different temperatures.



(**a**) (**b**)

Figure 18. Bubble size and porosity distributions for the cases with same gas properties. (**a**) Bubble diameter over height for cases with same gas properties. (**b**) PDF of porosity for cases with same gas properties.

The second set of simulations explores the bubbling fluidization at different temperatures (see Section 4.2.1), accounting for the associated changes in gas properties. Figures 19 and 20 reproduce the experimental findings from Campos Velarde [8], while Figures 21 and 22 show the corresponding results from our CFD–DEM simulations. The simulations showed a decrease in particle circulation between 293 K and 373 K, as presented in Figure 21. However, this trend differs from the experiments, where the particle velocity did not change much at such (relatively) low temperatures, and it even showed an increase as the temperature rose from 473 K to 573 K (see Figure 19). This mismatch is further illustrated by the particle velocity profiles at various heights. The experimental data indicate an increase in the solid circulation intensity with temperature (Figure 20), while the simulations demonstrate a flattening of the profiles as temperature rises (Figure 22). The reduction in the particle circulation observed in the simulations aligns with the larger bubble sizes predicted at higher temperatures (Figure 23a). In this case, the bubble size trend agrees with the experimental results presented in Campos Velarde [8]. Similarly, the probability distribution function of the time-averaged bed porosity presented in Figure 24 shows that, at higher temperatures, gas bubbles are more prevalent, while the emulsion phase occurs less frequently. It should be noted that the voidage in the emulsion phase remains constant at approximately 0.4 but occurs less frequently.

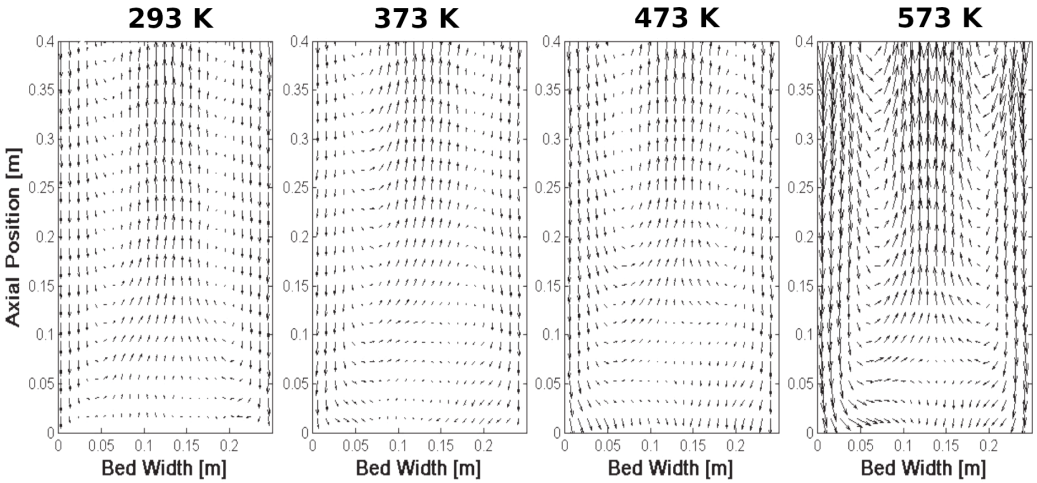


Figure 19. Solid circulation patterns of 400–600 µm glass beads fluidized with nitrogen at the same excess velocity at different operating temperatures; experiments by Campos Velarde [8].

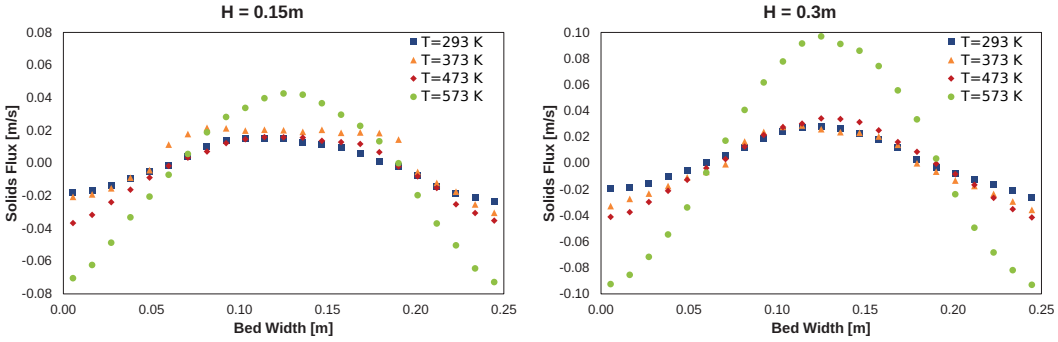


Figure 20. Time-averaged lateral solid velocity profiles at two positions above the porous plate fluidized with nitrogen at different temperatures; experiments by Campos Velarde [8].

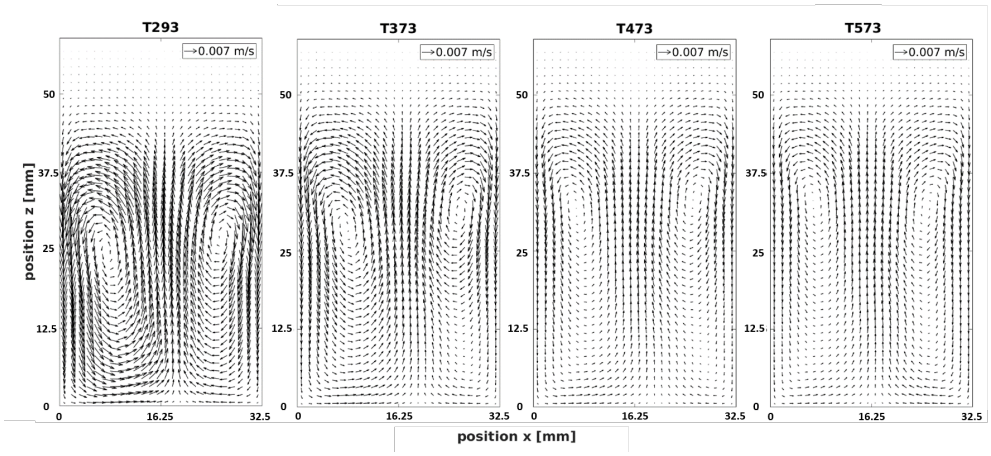
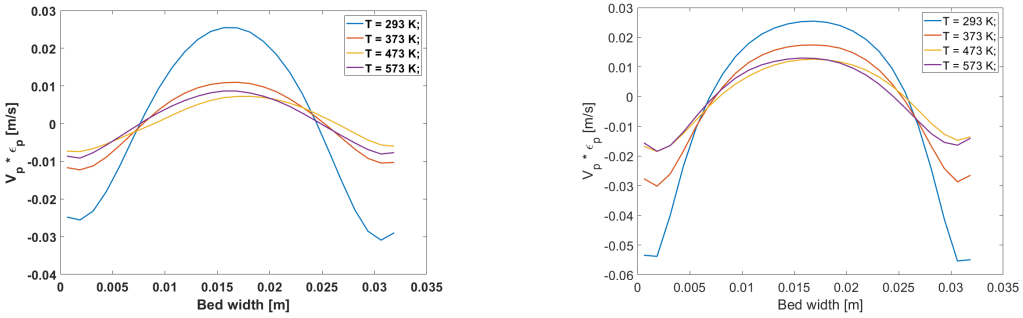


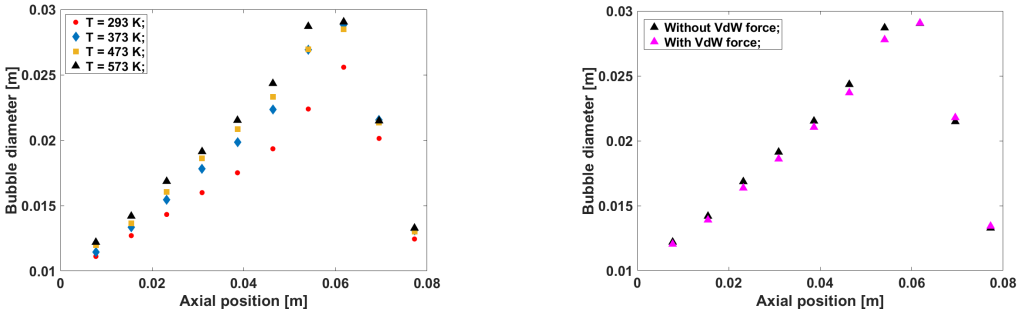
Figure 21. Time-averaged glass particle phase velocity for different temperatures.

The observed increase in particle circulation at higher temperatures in the experiments by Campos Velarde [8] cannot be explained by modifying the friction coefficient alone. In fact, as shown in the first part of this study, further increasing the friction coefficient would reduce the particle velocity, potentially contributing to the discrepancy between the simulations and experiments. Improved alignment could be achieved by reducing the normal restitution coefficient, which would be consistent with the expected changes in this particle property at higher temperatures and the conclusions reached in this study.



(**a**) Quarter height of the bed. (**b**) Middle height of the bed.

Figure 22. Particle velocity profiles at different heights of the bed for different temperatures.



(**a**) (**b**)

Figure 23. Bubble size distributions for glass particle fluidization for different temperatures with(out) VDW force. (**a**) Bubble diameter over height for glass particle fluidization. (**b**) Bubble diameter over height for glass particle fluidization for 573 K.

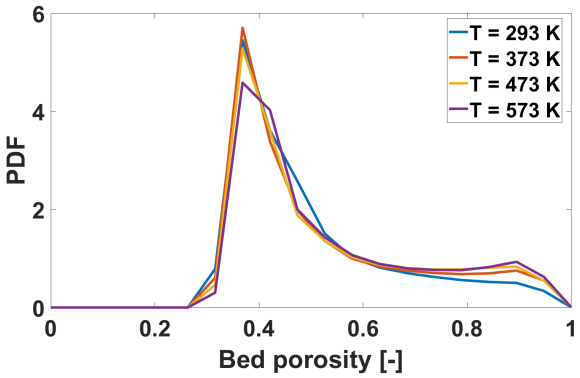


Figure 24. PDF of porosity for cases with different temperatures and variable gas properties.

In terms of VDW forces, studies by Formisani et al. [4], Campos Velarde [8] suggest that an increase in temperature strengthens these forces. Although an increase in temperature increases the bubble size (Figure 23a), simulations including VDW forces at 573 K show merely a reduction in the bubble size (Figure 23b) and no corresponding increase in particle velocity. This implies that, although this VDW force strength (F_{vdw} = 2*F_g) was sufficient to influence the minimum fluidization velocity, its effect remains minimal during bubbling fluidization. The precise relationship between VDW force strength and temperature therefore remains challenging to determine through tailoring the collisional properties. Until more data become available, this force should be considered as an additional parameter for the simulation that has to be adjusted based on the experimental observations.

5. Conclusions

Fluidization hydrodynamics can change significantly because of the effect that temperature has on the properties of the particles and gases, thus affecting the overall fluidization behavior. To quantify these effects, the results of CFD–DEM simulations that examined the influence of particle collisional properties on the fluidization behavior from minimal fluidization velocity to a bubbling fluidized bed were presented. The main focus was to highlight the relative importance of the temperature dependency of the gas properties, particle collisional parameters, and inter-particle forces. The initial simulations were performed to assess the influence of the collisional parameters, from which it was concluded that the coefficient of friction is the main parameter that determines the minimal fluidization velocity because of its large influence on the packed bed porosity.

The normal restitution coefficient has a small influence on the minimal fluidization conditions, whereas the tangential restitution coefficient, in all the simulations that were performed, has a negligible influence, at least for the cases investigated in this work.

Simulations with fully bubbling fluidization showed that both friction and normal restitution contribute to the hydrodynamic behavior inside the reactor. A lower normal restitution coefficient resulted in a larger bubble size, which, in turn, increased the particle circulation. Increasing the friction coefficient facilitates decreases in bubble size and corresponding reductions in particle velocity intensity. Here, too, the tangential restitution coefficient demonstrated a negligible effect.

The second part of the paper involved a comparison study of numerical simulations with experimental data from Campos Velarde [8]. The fluidization behavior was investigated at different temperatures. In order to reproduce the experiments, the collisional parameters were fitted to match the minimum fluidization velocities measured. It has been shown that, if the collisional properties are not corrected for a change in temperature, the simulations will under-predict the values for U_{mf}. The main tuning parameter was found to be the friction coefficient; the restitution coefficients had much less of an influence on the minimum fluidization velocity.

Throughout this study, it was observed that the minimum fluidization velocity stabilizes with a further increase in the friction coefficient by reaching the highest packed bed porosity value. This finding indicates that an inter-particle interaction force needs to be included in order to reproduce the experimental data for elevated temperatures. Those experiments that exhibited an increase in particle velocity at higher temperatures can only be described by accounting for an attractive inter-particle force, which in this work was modeled as a VDWforce. However, a decrease in the normal restitution coefficient also presented a slight increase in the particle velocity.

In summary, the most critical temperature-dependent parameters that should be considered for accurately describing high-temperature fluidization in CFD–DEM simulations are the particle friction coefficient and gas properties, followed by the normal restitution coefficient and VDW forces. Only by combining all these factors can most of the experimental findings be reproduced, except at the highest temperature of 573 K.

Our discussion showed that obtaining accurate results at each fixed temperature in the system required different values for the particle collision properties (e.g., friction coefficient). However, in a fluidized bed, the temperature can change dynamically over time, and its influence on the particle collision parameters may differ between particles. While a general solution to this complex challenge is beyond the scope of this study, our findings highlight the need for further experimental and numerical investigations.

Author Contributions: Conceptualization, M.M., I.R. and M.V.S.A.; methodology, M.M.; software, M.M.; validation, M.M.; formal analysis, M.M. and J.G.R.; investigation, M.M., I.C.V., I.R. and M.V.S.A.; resources, I.R.; data curation, M.M. and J.G.R.; writing—original draft preparation, M.M. and I.R.; writing—review and editing, M.M., J.G.R., M.V.S.A. and I.R.; visualization, M.M. and J.G.R.; supervision, I.R. and M.V.S.A.; project administration, I.R.; funding acquisition, M.V.S.A. All authors have read and agreed to the published version of the manuscript.

Funding: This project has received funding from the European Union's Horizon 2020 research and innovation program under grant agreement No 680565, "Intensified by Design." https://doi.org/10.3030/680565 (accessed on 20 February 2025).

Data Availability Statement: The raw data supporting the conclusions of this article will be made available by the authors on request.

Conflicts of Interest: The authors declare no conflicts of interest. The funding agency had no role in the design of the study; in the collection, analyses, or interpretation of data; in the writing of the manuscript; or in the decision to publish the results.

Abbreviations

The following abbreviations are used in this manuscript:

CFD	Computational Fluid Dynamics
DEM	Discrete Element Method
PDF	Probability Density Function
VDW	Van der Waals

Nomenclature

Roman symbols	
A	Hamaker constant
C_D	drag coefficient
e_n	coefficient of normal restitution
e_t	coefficient of tangential restitution
f^a_{cell}	volume fraction of the particle in the Eulerian cell
$\mathbf{F}$	force, N
$\mathbf{g}$	gravity, m/s^2
$\mathbf{I}$	unit matrix
k	spring stiffness, N/m
P_g	pressure, Pa
m_i	particle mass, kg
m_{eff}	effective mass, kg
M	gas molecular weight, kg/mol
$\mathbf{n}_{ab}$	normal unit vector
$\mathbf{r}_i$	particle position, m
R_i	particle radius, m
S	inter-surface distance between two particles, m
$\mathbf{S}_p$	momentum transfer source term, N/m^3
$\mathbf{u}_g$	gas velocity, m/s
$\mathbf{v}_i$	particle velocity, m/s
U_{mf}	minimum fluidization velocity, m/s
V_i	particle volume, m^3

Greek symbols	
β	inter-phase momentum transfer coefficient, kg/(m^3 s)
ε_g	gas volume fraction
δ	displacement, m
μ_g	gas viscosity, kg/(m s)
μ_f	particle friction coefficient
η	damping coefficient, N (s/m)
λ_g	gas bulk viscosity, kg/(m s)
ρ_g	gas density, kg/m^3
ρ_p	particle density, kg/m^3
τ_g	stress tensor, Pa
ω_i	particle angular velocity, s^{-1}
Subscripts	
0	prior to collision
a, b	particle indices
n	normal direction
t	tangential direction

References

1. Geldart, D. Types of Fluidization. *Powder Technol.* **1973**, *7*, 285–292. [CrossRef]
2. Lettieri, P.; Newton, D.; Yates, J. High temperature effects on the dense phase properties of gas fluidized beds. *Powder Technol.* **2001**, *120*, 34–40. [CrossRef]
3. Botterill, J.; Teoman, Y.; Yüregir, K. The effect of operating temperature on the velocity of minimum fluidization, bed voidage and general behaviour. *Powder Technol.* **1982**, *31*, 101–110. [CrossRef]
4. Formisani, B.; Girimonte, R.; Mancuso, L. Analysis of the fluidization process of particle beds at high temperature. *Chem. Eng. Sci.* **1998**, *53*, 951–961. [CrossRef]
5. Shabanian, J.; Chaouki, J. Effects of temperature, pressure, and interparticle forces on the hydrodynamics of a gas–solid fluidized bed. *Chem. Eng. J.* **2017**, *313*, 580–590. [CrossRef]
6. Mihajlovic, M.; Roghair, I.; van Sint Annaland, M. High temperature fluidization - influence of inter-particle forces on fluidization behavior. In Proceedings of the 12th International Conference on Computational Fluid Dynamics in the Oil & Gas, Metallurgical and Process Industries, Trondheim, Norway, 30 May–1 June 2017; Olsen, J., Johansen, S., Eds.; SINTEF Academic Press: Oslo, Norway, 2017; pp. 107–114.
7. Laverman, J.; Roghair, I.; Annaland, M.; Kuipers, H. Investigation into the hydrodynamics of gas–solid fluidized beds using particle image velocimetry coupled with digital image analysis. *Can. J. Chem. Eng.* **2008**, *86*, 523 – 535. [CrossRef]
8. Campos Velarde, I. High Temperature Hydrodynamics for Chemical Looping Biomass Gasification. Ph.D. Thesis, Eindhoven University of Technology, Eindhoven, The Netherlands, 2016.
9. Krupp, H. Particle adhesion theory and experiment. *Adv. Colloid Interface Sci.* **1967**, *1*, 111–239. [CrossRef]
10. Lawrence, M.J.; Bons, J.; Lawrence, J.; Lawrence, B.; Whitaker, S.; Casaday, B.; Clum, C.; Bonilla, C.; Lawrence, M.; Lageman, D.; et al. An Experimental Investigation of High Temperature Particle Rebound and Deposition Characteristics Applicable to Gas Turbine Fouling. Master's Thesis, The Ohio State University, Columbus, OH, USA, 2013.
11. Mok, C.; Duffy, J. The behavior of metals at elevated temperatures under impact with a bouncing ball. *Int. J. Mech. Sci.* **1964**, *6*, 161–175. [CrossRef]
12. Brenner, S.; Wriedt, H.; Oriani, R. Impact adhesion of iron at elevated temperatures. *Wear* **1981**, *68*, 169–190. [CrossRef]
13. Hashemnia, K. Experimental study of the effect of temperature on the coefficient of restitution of steel balls impact to some industrial metal sheets at elevated temperatures. *Powder Technol.* **2020**, *368*, 170–177. [CrossRef]
14. Diani, J.; Gilormini, P.; Agbobada, G. Experimental study and numerical simulation of the vertical bounce of a polymer ball over a wide temperature range. *J. Mater. Sci.* **2014**, *49*, 2154–2163. [CrossRef]
15. Dong, M.; Xie, J.; Bai, L.; Li, S. An Experimental Investigation on the Influence of Temperature on the Normal Impact of Fine Particles with a Plane Surface. *Energies* **2014**, *7*, 2079–2094. [CrossRef]
16. Li, A.; Li, X.; Xu, X.; Zhang, Y.; Zhu, L.; Liu, P. Numerical modeling of wall-to-cluster heat transfer in swirling fluidized beds based on MFiX-DEM approach. *Case Stud. Therm. Eng.* **2025**, *65*, 105634. [CrossRef]
17. Patil, A.V.; Peters, E.A.; Kolkman, T.; Kuipers, J.A. Modeling bubble heat transfer in gas-solid fluidized beds using DEM. *Chem. Eng. Sci.* **2014**, *105*, 121–131. [CrossRef]

18. Schirck, J.; Appaswamy, K.; Morris, A.; Ma, Z. Inhomogeneous temperature in high temperature fluidized beds. *Powder Technol.* **2024**, *434*, 119354. [CrossRef]
19. Lan, B.; Xu, J.; Lu, S.; Liu, Y.; Xu, F.; Zhao, B.; Zou, Z.; Zhai, M.; Wang, J. Direct reduction of iron-ore with hydrogen in fluidized beds: A coarse-grained CFD-DEM-IBM study. *Powder Technol.* **2024**, *438*, 119624. [CrossRef]
20. Liu, X.; Hessels, C.J.; Deen, N.G.; Tang, Y. CFD-DEM investigation on the agglomeration behavior of micron-sized combusted iron fines. *Fuel* **2023**, *346*, 128219. [CrossRef]
21. Chen, Z.; Jiang, L.; Qiu, M.; Chen, M.; Liu, R.; Liu, M. Cfd-dem simulation of spouted bed dynamics under high temperature with an adhesive model. *Energies* **2021**, *14*, 2276. [CrossRef]
22. Kuwagi, K.; Mikami, T.; Horio, M. Numerical simulation of metallic solid bridging particles in a fluidized bed at high temperature. *Powder Technol.* **2000**, *109*, 27–40. [CrossRef]
23. Laverman, J. On the Hydrodynamics in Gas Phase Polymerization Reactors. Ph.D. Thesis, Technische Universiteit Eindhoven, Eindhoven, The Netherlands, 2010. [CrossRef]
24. Hoomans, B.; Kuipers, J.; Briels, W.; van Swaaij, W. Discrete particle Simulation of Bubble and Slug Formation in a 2D Gas-Fluidised Bed: A Hard-Sphere Approach. *Chem. Eng. Sci.* **1996**, *51*, 99–118. [CrossRef]
25. van der Hoef, M.; Ye, M.; van Sint Annaland, M.; Andrews, A.; Sundaresan, S.; Kuipers, J. Multiscale Modeling of Gas-Fluidized Beds. In *Computational Fluid Dynamics*; Marin, G.B., Ed.; Academic Press: Cambridge, MA, USA, 2006; Volume 31; Advances in Chemical Engineering; pp. 65–149. [CrossRef]
26. Ye, M.; van der Hoef, M.; Kuipers, J. A numerical study of fluidization behavior of Geldart A particles using a discrete particle model. *Powder Technol.* **2004**, *139*, 129–139. [CrossRef]
27. Tan, L. Discrete Particle Simulations of Micro-Structured Membrane-Assisted Fluidized Beds. Ph.D. Thesis, Eindhoven University of Technology, Eindhoven, The Netherlands, 2015.
28. Cundall, P.; Strack, O. A Discrete Numerical Model for Granualar Assemblies. *Geotechnique* **1979**, *29*, 47–65. [CrossRef]
29. Syamlal, M.; Gidaspow, D. Hydrodynamics of fluidization: Prediction of wall to bed heat transfer coefficients. *AIChE J.* **1985**, *31*, 127–135. [CrossRef]
30. Johnson, K. *Contact Mechanics*; Cambridge University Press: Cambridge, UK, 1985. [CrossRef]
31. Ye, M. Multi-Level Modeling of Dense Gas-Solid Two-Phase Flows. Ph.D. Thesis, University of Twente, Enschede, The Netherlands, 2005.
32. Ye, M.; van der Hoef, M.; Kuipers, J. From discrete particle model to a continuous model of Geldart a particles. *Chem. Eng. Res. Des.* **2005**, *83*, 833–843. [CrossRef]
33. Hamaker, H. The London-van der Waals attraction between spherical particles. *Physica* **1937**, *4*, 1058–1072. [CrossRef]
34. Israelachvili, J. *Intermolecular and Surface Forces*; Academic Press: Cambridge, MA, USA, 2011.
35. Hunter, R. *Foundations of Colloid Science*, 2nd ed.; Oxford University Press: Oxford, UK, 2001. [CrossRef]
36. Gidaspow, D. *Multiphase Flow and Fluidization: Continuum and Kinetic Theory Descriptions*; Academic Press Limited: Cambridge, MA, USA, 1994; pp. 1–467. [CrossRef]
37. Ergun, S. Fluid flow through packed columns. *Chem. Eng. Prog.* **1952**, *48*, 89–94.
38. Wen, Y.; Yu, Y. Mechanics of Fluidization. *Chem. Eng. Prog. Symp. Ser.* **1966**, *62*, 100–111.
39. Bird, R.; Stewart, W.; Lightfoot, E. *Transport Phenomena*, 2nd ed.; John Wiley & Sons, Inc.: Hoboken, NJ, USA, 2002; p. 566.
40. Tan, L.; Roghair, I.; van Sint Annaland,, M. Simulation study on the effect of gas permeation on the hydrodynamic characteristics of membrane-assisted micro fluidized beds. *Appl. Math. Model.* **2014**, *38*, 4291–4307. [CrossRef]
41. Kuipers, J.; Van Duin, K.; Van Beckum, F.; Van Swaaij, W. A numerical model of gas-fluidized beds. *Chem. Eng. Sci.* **1992**, *47*, 1913–1924. [CrossRef]
42. Kunii, D.; Levenspiel, O.; Brenner, H. *Fluidization Engineering*, 2nd ed.; Butterworth-Heinemann-series in chemical engineering; Elsevier Science: Amsterdam, The Netherlands, 1991.
43. Hoomans, B. Granular Dynamics of Gas-Solid Two-Phase Flows. Ph.D. Thesis, University of Twente, Enschede, The Netherlands, 2000.
44. Kozeny, J. Ueber kapillare Leitung des Wassers im Boden. *Sitzungsber Akad. Wiss. Wien* **1927**, *136*, 271–306.
45. Carman, P. Fluid flow through granular beds. *Trans. Inst. Chem. Eng. Lond.* **1937**, *15*, 150–166. [CrossRef]
46. Carman, P. *Flow of Gases Through Porous Media*; Butterworths: London, UK, 1956.
47. Subramani, H.J.; Mothivel Balaiyya, M.; Miranda, L.R. Minimum fluidization velocity at elevated temperatures for Geldart's group-B powders. *Exp. Therm. Fluid Sci.* **2007**, *32*, 166–173. [CrossRef]
48. Seville, J.; Willett, C.; Knight, P. Interparticle forces in fluidisation: A review. *Powder Technol.* **2000**, *113*, 261–268. [CrossRef]

Disclaimer/Publisher's Note: The statements, opinions and data contained in all publications are solely those of the individual author(s) and contributor(s) and not of MDPI and/or the editor(s). MDPI and/or the editor(s) disclaim responsibility for any injury to people or property resulting from any ideas, methods, instructions or products referred to in the content.